ADVANCED ENERGY MATERIALS
www.advenergymat.de

Predicting Molecular Ordering in Deposited Molecular Films

*Christoph Scherer, Naomi Kinaret, Kun-Han Lin, Muhammad Nawaz Qaisrani, Felix Post, Falk May, and Denis Andrienko**

Thin films of molecular materials are commonly employed in organic light-emitting diodes, field-effect transistors, and solar cells. The morphology of these organic films is shown to depend heavily on the processing used during manufacturing, such as vapor co-deposition. However, the prediction of processing-dependent morphologies has until now posed a significant challenge, particularly in cases where self-assembly and ordering are involved. In this work, a method is developed based on coarse-graining that is capable of predicting molecular ordering in vapor-deposited films of organic materials. The method is tested on an extensive database of novel and known organic semiconductors. A good agreement between the anisotropy of the refractive indices of the simulated and experimental vapor-deposited films suggests that the method is quantitative and can predict the molecular orientations in organic films at an atomistic resolution. The methodology can be readily utilized for screening materials for organic light-emitting diodes.

1. Introduction

Thin films of molecular materials are commonly used in organic light-emitting diodes,[1,2] field-effect transistors,[3] and solar cells.[4] Fine-tuning the chemical composition of these films can be a time-consuming process, as there is often no discernible correlation between the molecular structure and the resulting electronic properties. Simulating film properties can aid in this process, provided that the simulations are both feasible and accurate. The prediction of energetic disorder and charge carrier mobilities, for example, has been shown to be possible in completely amorphous or perfectly crystalline systems.[5–8] However, the prediction of processing-dependent morphologies still poses a significant challenge, particularly in films with partial molecular ordering.[9–12]

The morphology of organic films has been shown to depend on the conditions during vapor co-deposition (VD), one of the most commonly used production methods in industry.[10,13,14] In deposited films several key factors influence molecular packing, these include the VD deposition rate, the nature of the substrate, and the substrate temperature. The experimental deposition rate typically falls within the range of 1 Å s^{-1}, whereas the deposition rates that can be achieved with atomistic molecular dynamics simulations are below 10^{-9} Å s^{-1}.[15] Therefore, it is practically impossible to accurately mimic the experimental conditions and simulate the film morphology, as this depends on the deposition rate. Indeed, previous works have shown that all-atom (AA) VD simulation protocols are only capable of predicting film morphologies that correspond to high deposition rates, primarily with a face-on molecular orientation.[9]

Thankfully, direct replication of the experimental conditions is also unnecessary. Ad hoc coarse-grained (CG) models have been shown to be capable of capturing the molecular orientation in thin films produced through VD.[10,11] Coarse-grained models tend to have a smoother potential energy landscape, thus resulting in intrinsically faster dynamics, making deposition rates of 10^{-6} Å s^{-1}, on the order of the molecular diffusion on, and into, the film surface, achievable.[15] CG models, however, often do not retain enough chemical information to allow for the reintroduction of atomistic details or to accurately model intermolecular interactions. Without a direct comparison to experimental results, it is thus unclear whether this approach can be applied to a broader range of chemistries or how accurate and reliable the predictions are.

In this study, we demonstrate that CG models, which have been parametrized on atomistic simulations, are capable of accurately predicting molecular alignment in thin films across a broad range of molecular species. By reintroducing atomistic details, we can compare the anisotropy of the refractive index computed by our models with experimental measurements, revealing a robust correlation between the simulated and experimentally determined values. Our study represents a significant step toward a long-awaited approach that, when combined with perturbative schemes,[16,17] could provide reliable values for ionization energies and electron affinities,[5,16,17,18] absorption and emission spectra,[19,20] electronic density of states,[5,18] or glass transition temperatures.[21]

C. Scherer, N. Kinaret, K.-H. Lin, M. N. Qaisrani, F. Post, D. Andrienko
Max Planck Institute for Polymer Research
Ackermannweg 10, 55128 Mainz, Germany
E-mail: denis.andrienko@mpip-mainz.mpg.de
F. May
Merck Electronics KGaA
64293 Darmstadt, Germany

The ORCID identification number(s) for the author(s) of this article can be found under https://doi.org/10.1002/aenm.202403124

DOI: 10.1002/aenm.202403124

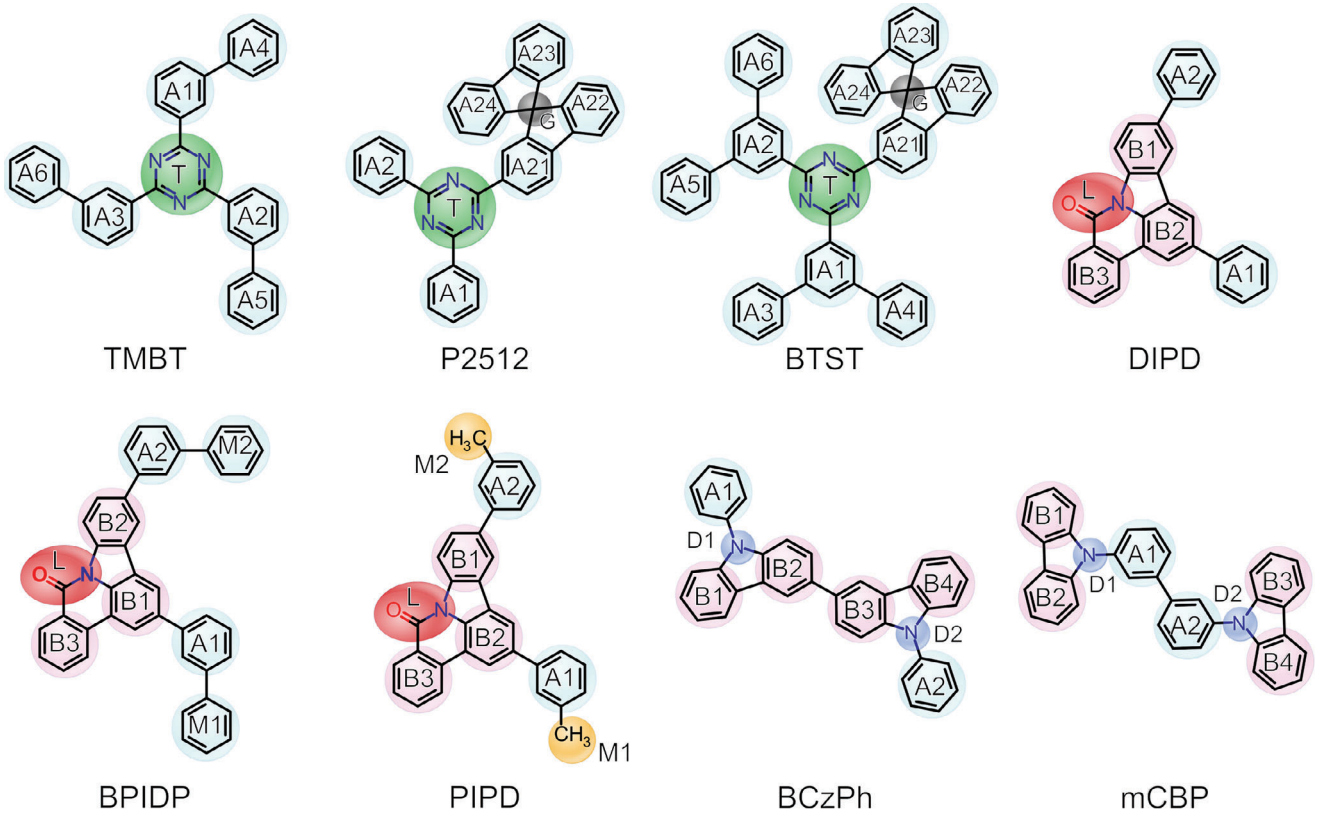

Figure 1. Chemical structures and coarse-grained mappings of the studied molecules. The different bead colors represent the different bead types used in the coarse-grained scheme.

2. Results and Discussion

In this work, we consider a set of eight different transport or host materials for organic light-emitting diodes: BTST, P2512, BCzPh, mCBP, DIPD, BPIDP, PIPD, and TMBT. These molecules were chosen as they cover a wide range of glass transition temperatures and anisotropies of the refractive indices. This is important as we need to show that the method presented in this workflow holds for molecules that require different processing conditions and have different morphologies and degrees of ordering in the final VD film. The chemical structures, and the CG mappings of these molecules are shown in **Figure 1**.

The developed methodology is described in **Figure 2**. The adapted atomistic force field is used to parametrize the coarse-grained model, as described in the Experimental Section. The corresponding glass transition temperatures, T_g^{AA}, T_g^{CG}, and T_g^{exp}, summarized in **Table 1**, are evaluated or measured experimentally as described in the Experimental Section. The correlations of the different glass transition temperatures are shown in **Figure 3**. It is clear from Table 1 that the T_g^{AA} values are correlated but overestimate T_g^{exp}, in line with the findings of Lin et al.[21] As expected, T_g^{CG} are lower than the all-atom (AA) values due to the softening of potentials and smoothing of the potential energy landscape associated with coarse-graining, yielding intrinsically faster dynamics. For T_g^{CG} no correlation is expected, as coarse-graining arbitrarily enhances molecular diffusion.

The deposition simulation itself is then performed at CG resolution by iteratively inserting new molecules above the substrate. After each insertion step, the newly inserted molecules are cooled to the substrate temperature over time t_d allowing them to diffuse over and into the film surface. This insertion process is repeated until the desired film thickness of up to 20 nm is achieved. The final step of our workflow reintroduces atomistic details into coarse-grained morphologies, as described in the Experimental section. These morphologies are then used to calculate the difference between the extraordinary and ordinary refractive indices, $\Delta n = n_e - n_o$, as summarized in the Experimental Section.

2.1. Influence of the Deposition Rate and Substrate Temperature

To probe the orientation of molecules within the deposited films, we use a nematic order parameter,[22] $S_z = \frac{1}{2}\langle 3(\boldsymbol{\mu}\cdot\boldsymbol{e}_z)^2 - 1\rangle$, where $\rangle\cdots\langle$ denotes the ensemble average, $\boldsymbol{\mu}$ is a vector perpendicular to the molecular plane, and $\boldsymbol{e}_z$ is the unit vector perpendicular to the substrate. S_z can be used to determine whether molecules in the deposited film are on average standing upright or lying flat relative to the film surface. $S_z = -0.5$ corresponds to a system where all vectors $\boldsymbol{\mu}$ are aligned in the xy plane, while $S_z = 1$ corresponds to the vectors $\boldsymbol{\mu}$ aligning parallel, or antiparallel, to the substrate normal.

The effect of deposition equilibration time t_d is presented in **Figure 4** for two typical compounds, BTST and DIPD. It is clear

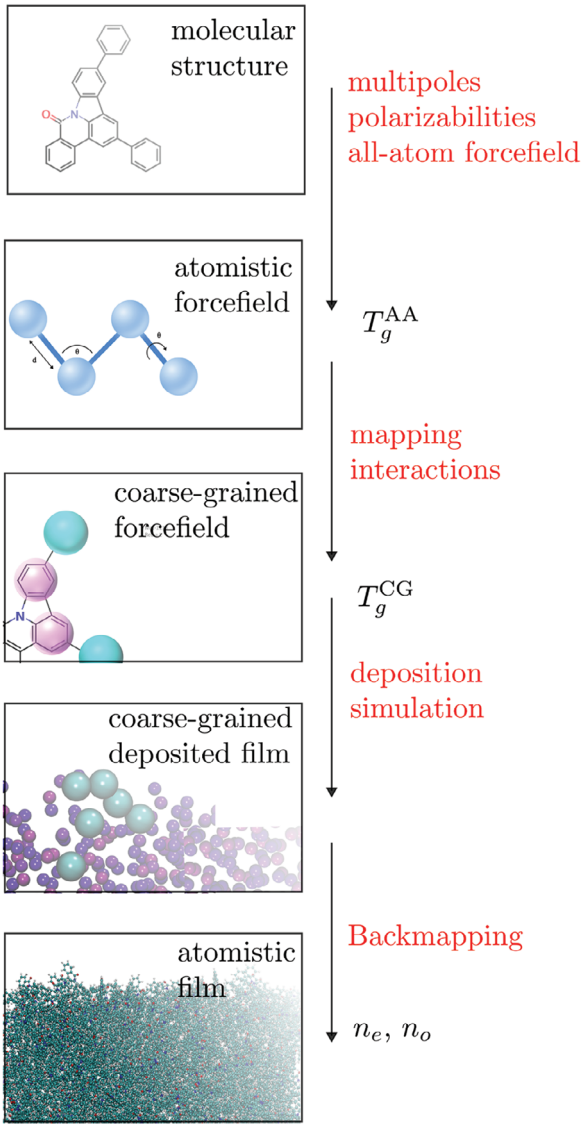

Figure 2. Workflow for morphology prediction of deposited organic thin films. The molecular structure is first optimized and atomic charges, multipoles, and molecular polarizability are calculated and incorporated into atomistic/polarizable force fields. These force fields allow us to probe glass transition temperatures and distributions of inter- and intra-molecular degrees of freedom. Direct Boltzmann inversions and iterative Boltzmann inversions are utilized to parametrize bonded and non-bonded interactions, respectively, in the CG model. Deposition simulations are then performed at a CG resolution by iteratively inserting new molecules above the substrate. The final step reintroduces atomistic details into coarse-grained morphologies. These morphologies are subsequently used to calculate the difference between the extraordinary and ordinary refractive indices using the polarizable force field.

that changing the equilibration time has a significant impact on molecular orientations within the film, emphasizing that molecular alignment is a dynamic process. For $t_d = 10$ ns both systems appear to have reached an acceptable degree of saturation in a reasonable computational time, with a single film deposited in approximately one week on a 20-core machine. As such, all further deposition simulations in this work were carried out with an equilibration time of 10 ns. At this stage, it is also becoming clear why atomistic models, with their extremely fast deposition rates, fail to predict molecular orientations in VD films.

The substrate temperature T_{dep}^{CG} is also found to have a significant effect on the observed S_z values of the systems, Figure 4. A general trend was observed across all systems where molecules tend toward a lying flat orientation at lower substrate temperatures and an amorphous structure, with $S_z = 0$, at high temperatures. In the case of DIPD, the molecular orientation changes from flat-lying at low deposition temperatures to upright standing at intermediate temperatures and finally to an amorphous morphology at high temperatures, close to or above T_g. The orientation of BTST is found to gradually change from lying flat to amorphous. All the studied compounds exhibited one of two characteristic behaviors.

This is attributed to the significantly slower dynamics at lower temperatures resulting in the "flat-lying" surface structure observed in films deposited at an all-atom resolution. However, in the intermediate temperature region, around T_g^{CG}, the ordering of molecules within the film differs significantly between the systems. Some of the systems display strong ordering, like TMBT, which has a significant proportion of molecules standing upright within the bulk film, while others, like mCBP, remain amorphous across the entire temperature range.

2.2. Generic Rate Model

The change in film morphology due to variations in deposition temperature and rate can be explained by a rate model that assumes that molecules landing on the top of the film are first mobile. The mobile molecules are frozen into place when the local density becomes too high due to continued deposition. To account for the faster diffusion of upright-standing molecules into the film, as compared to that of flat-lying molecules, we choose to include the free energy barrier for the rotational motion of mobile molecules from flat-lying to upright-standing. The corresponding rate equations, and their solution, are provided in the ipython notebook (see the Data Availability Section). The key result of this model is that the nematic order parameter S of molecular orientations in the film is a weighted sum of the order parameters of flat-lying and upright-standing molecules,

Table 1. Glass transition temperatures: experimentally measured (T_g^{exp}), all-atom (T_g^{AA}) and coarse-grained (T_g^{CG}) models. T_{dep}^{CG} is the film deposition temperature, and Δn^{exp} and Δn^{sim} are the experimentally measured and calculated anisotropies of the refractive indices, respectively.

	T_g^{exp} [K]	T_g^{AA} [K]	T_g^{CG} [K]	T_{dep}^{CG} [K]	Δn^{exp}	Δn^{sim}
BTST	433	486	347	247	−0.17	−0.11
P2512	408	480	264	199	−0.07	−0.02
BCzPh	371	446	237	197	−0.04	−0.04
mCBP	366	442	224	189	0.00	0.03
DIPD	366	453	295	248	0.08	0.13
BPIDP	379	432	301	240	−0.12	−0.07
PIPD	351	419	276	180	0.13	0.06
TMBT	330	362	277	259	0.14	0.15

$S(T) = [S_f(T) + \eta S_u(T)]/[1 + \eta]$. The weight $\eta = I\omega_{f\to u/\Omega}$ is proportional to the rate of molecular reorientation from flat-lying to upright-standing, $\omega_{f\to u}$, and is inversely proportional to the deposition rate Ω. I is the (fixed) thickness of the monolayer of mobile molecules.

When the deposition rate is much higher than the rate of rotational diffusion (small η), the molecules are lying flat on the surface. This scenario corresponds to, for example, an all-atom deposition simulation, which has an artificially fast deposition rate. If the deposition rate is comparable to the rate of molecular reorientation, some molecules will change their orientation from flat-lying to upright-standing before becoming immobile. Because a temperature increase promotes rotational motion, the number of upright-standing molecules can be increased either by decreasing the deposition rate or increasing the deposition temperature. There is, however, no simple scaling relation between these two parameters, since $\omega_{f\to u} \approx \omega^0_{f\to u} \exp[-\frac{\Delta U_{f\to u}}{k_B T_{dep}}]$. At temperatures close to T_g the films become amorphous due to the broadening of the orientational distribution functions of both upright-standing and flat-lying molecules. From this, it is clear that the optimal deposition temperatures are just below T_g as this allows efficient reorientation of molecules from flat lying to upright standing, facilitating diffusion into the film, while still maintaining a narrow enough orientational distribution function to preserve any ordering phenomena. This also accounts for the non-monotonous dependence of the order parameter S on the temperature, as shown in Figure 4 for DIPD: at low deposition temperatures rotational motion is limited, and flat-lying molecules dominate, while at higher temperatures upright standing molecules can more readily diffuse into the film, leading to negative S values, and ultimately observing amorphous films at T_g. If the activation barrier for the rotation from flat-lying to upright-standing molecules is too high, then no upright-standing films are formed, even at temperatures approaching T_g, as is the case for in BTST, Figure 4.

2.3. Accounting for the Difference in Dynamics Between Different Simulation Resolutions

The key observation here is that the ordering of the molecules changes significantly with the substrate temperature and deposition rate, reaffirming the importance of choosing the correct deposition temperature to accurately reproduce experimental film morphologies. This is because moving from the AA resolution to the CG resolution results in intrinsically faster dynamics, thus making it impossible to compare results obtained at the same absolute temperatures. Choosing the correct temperature for CG simulations is important because the morphology of deposited films relies on the interplay of both dynamics, the amount of time the molecules are given to structurally relax, and thermodynamics. Thus, it is important to quantify the change in dynamics that occurs when moving from the AA model to the CG model. This can be done by comparing the glass transition temperatures, T_g, of the system at different resolutions, as well as those obtained experimentally. The dynamics of different glass-forming liquids fall onto a generic curve, only dependent on the "fragility" of the glass-forming liquid when scaled with T_g.[23] Therefore, a scaled by T_g dimensionless temperature, T/T_g, can be used to relate the models across resolutions, as the fragility of

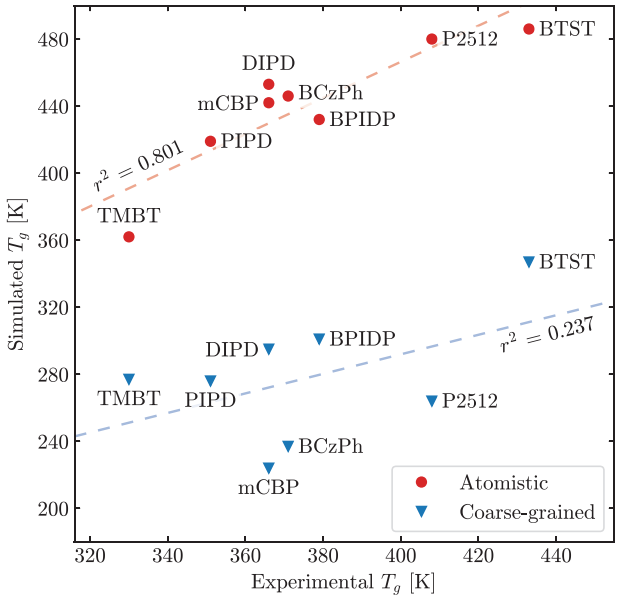

Figure 3. Correlation plot of the simulated and experimentally determined glass transition temperatures for the all-atom and coarse-grained models. The glass transition temperature of the atomistic model correlates well with experimentally measured values. The glass transition of the coarse-grained model depends on the degree of coarse-graining, which is impossible to control; thus, the correlation worsens.

the different resolutions should be the same. The same fragility should also apply to the experimental system, thus allowing us to use the dimensionless temperature to find the appropriate temperatures for comparison both between the AA and CG resolutions, as well as for comparisons between simulated and experimental data. Once all glass transition temperatures are calculated, we can determine the coarse-grained deposition temperature, $T^{CG}_{dep} = T^{exp}_{dep} T^{CG}_g / T^{exp}_g$, which ensures that the coarse-grained deposition dynamics agree with the experimental deposition conditions at $T^{exp}_{dep} = 308$ K. These temperatures are also summarized in Table 1.

2.4. Reintroduction of Atomistic Details and Refractive Index Calculations

To validate the suggested protocol, we compared the experimentally measured and simulated values of the anisotropy of the refractive indices, $\Delta n = n_e - n_o$ at 620 nm. Here, n_o is the ordinary refractive index within the xy plane, and n_e denotes the extraordinary refractive index, along the z-axis. Δn provides a measure of the anisotropy of each system, with a positive Δn indicating an on-average upright standing orientation and a negative value indicating that the molecules are on average lying flat. The experimental Δn values were determined as described in the Experimental Section.

To calculate the Δn values of the simulated deposited films atomistic details are reintroduced into the CG morphologies, as outlined in the Experimental Section. The refractive indices are then calculated using a polarizable Thole model[24] as outlined in the Experimental Section. The temperature dependencies of

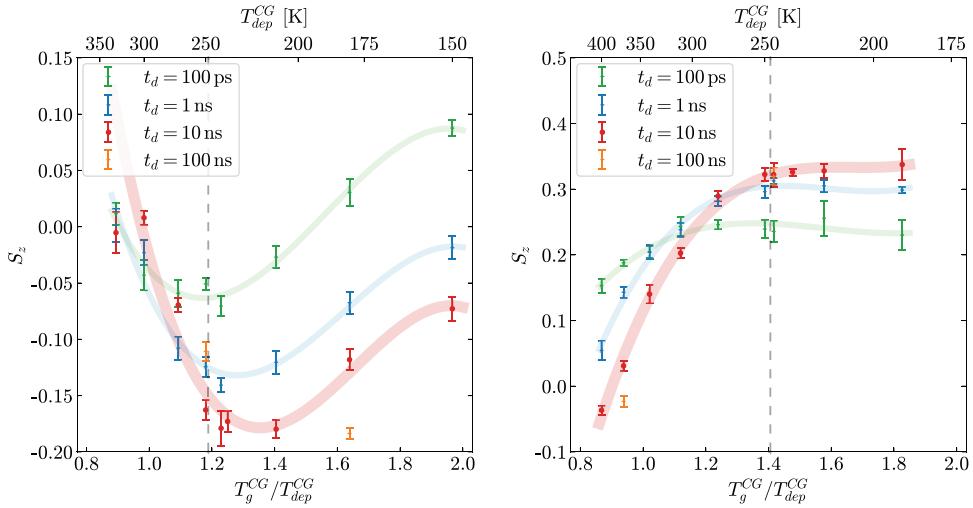

Figure 4. Deposition time dependence of S_z in DIPD (left) and BTST (right). $S_z < 0$ indicates that the molecular planes are perpendicular to the substrate plane (standing upright), $S_z = 0$ indicates isotropic morphologies, and $S_z > 0$ indicates that molecules are lying flat. Inserts show the molecular orientation at the CG deposition temperature corresponding to the experimental conditions, shown here as a dashed line. For each set of parameters, the deposition simulation was repeated five times using different random seeds, resulting in five independent films. The 100 ns deposition time is so computationally demanding that we can simulate only a few selected temperatures.

these refractive indices reflect the same trends as observed for the order parameter S_{zz}, with molecules on average lying flat at low temperature and tending toward amorphous at high temperatures.

When comparing the degree of ordering in films of different molecule types to the experimental results we consider the Δn values at the relevant deposition temperature T_{dep}^{CG}, given in Table 1. A robust correlation between these calculated Δn values and experimentally measured values is observed in **Figure 5**. The range of Δn, from very negative for BTST to very positive for TMBT, proves that the molecular orientations in deposited films are reproduced across a wide range of chemistries with reasonable accuracy.

Note that the proposed simulation protocol relies on the experimentally measured glass transition temperature. For materials that have not yet been synthesized, T_g^{exp} can be estimated from the correlation shown in Figure 3. This estimate makes the entire methodology ready for high-throughput material prescreening protocols.

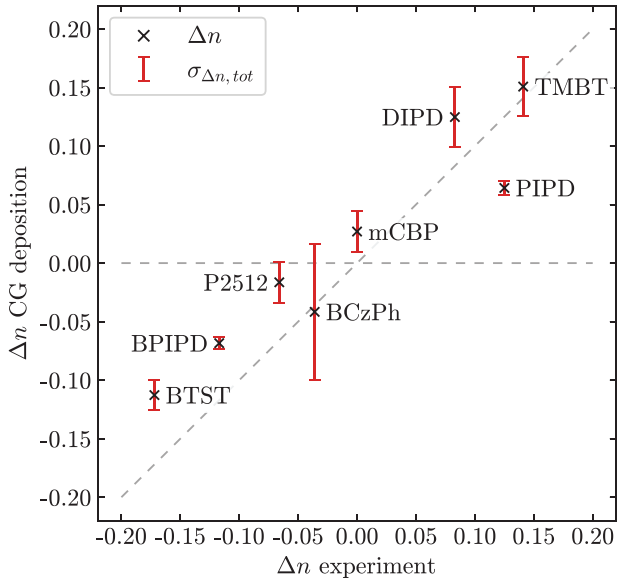

Figure 5. Correlation of simulated and measured values for $\Delta n = n_e - n_o$ with CG potentials parametrized from the OPLS+ force field.

3. Conclusion

In this work, we propose a method based on coarse-graining to predict the morphology of vapor-deposited thin films of organic materials. This method utilizes both Boltzmann and iterative Boltzmann inversions to parametrize coarse-grained force fields from atomistic ones. Glass transition temperatures are used to rescale temperatures and preserve dynamics between the two simulation models, as well as to accurately capture the dynamics under experimental deposition conditions. A deposition simulation can then be performed using the coarse-grained model by iteratively inserting additional molecules above the deposition substrate, allowing sufficient equilibration times before each sequential insertion step. A simple energy minimization backmapping scheme is then used to reintroduce atomistic details, allowing refractive index calculations to be performed. From the results presented above, we conclude that a good agreement between the experimentally measured and simulated refractive indices is achieved using the thin film morphologies obtained using our workflow. Thus, we conclude that one can reasonably predict the morphology of vapor deposited thin films of organic molecules using a coarse-grained model parametrized on atomistic force fields and temperatures that accelerate dynamics, making it possible to reproduce experimental conditions.

4. Experimental Section

Atomistic Force Field: To study the impact of force fields on the final coarse-grained models, two different types of atomistic force fields were considered in this work: OPLS+ and DDEC6.[25,26,27] The OPLS+ force field was an adaptation of the optimized potential for liquid simulations (OPLS) force field.[25,26] All Lennard–Jones parameters, as well as bonded parameters, were taken from this force field, and the OPLS combination rules were used with a fudge factor of 0.5 for 1–4 interactions. Atomic partial charges were computed via the Merz–Kollmann method by fitting the electrostatic potential of the electron density for DFT calculations performed at the B3LYP/6-31G(d) level.[28] For parametrization of dihedral potentials, the molecules were partitioned into rigid fragments.[29] By fitting fixed values of the dihedral angle between rigid fragments, the molecular geometry was optimized using the xTB package version 6.2.7. The resulting potential energy surface was then fitted to the Ryckaert–Belleman polynomial, $V_{RB}(\theta) = \sum_{n=0}^{5} C_n \cos^n\theta$. The DDEC6 force field also uses bond and angle parameters from the OPLS force field and utilizes the same OPLS combination rules with a fudge factor of 0.5 for 1–4 interactions.[25,26,30] However, here Lennard–Jones parameters and partial charges were derived following the protocol proposed by Cole et al.[31] The overlapping atomic electron densities were obtained via the density-derived electrostatic and chemical (DDEC6) electron density partitioning scheme.[10] The atomic partial charges can then be obtained by integrating the corresponding atomic electron densities over the whole space. Additionally, the two parameters, A and B, in the Lennard–Jones potential were then derived using the Tkatchenko–Scheffler (TS) scheme,[32] where the radius of the free atom in a vacuum was taken from the work of Cole et al.[31] The electron density was obtained using Gaussian 16[33] at the ωB97X-D[34]/6-311G(d,p) level, and the DDEC6 computations were performed using Chargemol version 09_26_2017.[27] The dihedral scan, performed with xTB for the OPLS+ force field, was done at the ωB97X-D[34]/6–311G(d,p) level using the Gaussian 16 package.[33,35]

Molecular Dynamics Simulations: All the AA simulations were performed at $P = 1.0$ bar using a Berendsen barostat[36] with a time constant of 0.5 ps, and a velocity rescaling thermostat[16] with a time constant of 0.5 ps and a compressibility of 4.5×10^{-5} bar^{-1}. A time step of 1 fs was used for all the atomic simulations. The electrostatic interactions were treated with a smooth particle mesh Ewald method with fourth-order cubic interpolation, 0.12 nm Fourier spacing, and an Ewald accuracy parameter of 10^{-5}. A short-range cutoff of $r_{cut} = 1.3$ nm was used and long-range dispersion corrections for energy and pressure were applied.

The coarse-grained *NVT* runs were performed using the velocity rescaling thermostat with a time constraint of 0.5 ps.[37] For the unconstrained simulations, a time step of 2 fs was used, while a 10 fs timestep was used for systems where bonds had been constrained using the fourth-order LINCS algorithm.[38] All the simulations were performed using GROMACS 2019.3[18,21,22] with the velocity rescaling thermostat with a time constant of 0.5 ps and the Berendsen barostat with a time constant of 0.5 ps.[37,36]

Coarse-Grained Force Field: For the CG models, a center of mass mapping was used, where M projects the atomistic configuration r to the coarse-grained resolution, such that each bead I was positioned at the center of mass R_I of all atoms i associated with it,

$$R_I = M_I(r) = \sum_{i \in \psi_I} c_{iI} r_i \tag{1}$$

where $c_{iI} = \frac{m_i}{\sum_{i \in \psi_I} m_i}$, ψ_I is the set of atomic indices corresponding to bead I, and r_i and m_i were the position and mass of atom i, respectively. The parametrization of CG force fields was based on matching distributions obtained from all atom *NVT* production runs, performed with either the OPLS+ or DDEC6 force fields outlined above. This was done using the software package Versatile Object-oriented Toolkit (VOTCA).[29]

Direct Boltzmann inversion (BI) was employed to parametrize the bonded interactions of the CG models,[39] while non-bonded interactions were obtained using iterative Boltzmann inversion (IBI).[40,41] Direct Boltzmann inversion assumes that the distribution for each independent variable q has the following form:

$$P_q(q) \propto \exp[-\beta U(q)], \ \beta = \frac{1}{k_B T_{\text{param}}} \tag{2}$$

It can then be inverted to obtain the CG potential of this variable, $U(q) = -k_B T_{\text{param}} \ln(P_q(q)) + \text{const.}$, where $q = r, \theta, \varphi$. Due to the construction of the software package, all correlations between different degrees of freedom were neglected. The histograms of bonds $H_r(r)$, angles $H_\theta(\theta)$ and dihedrals $H_\varphi(\varphi)$ must be normalized to obtain the correct distribution functions: $P_r(r) = \frac{H_r(r)}{4\pi r^2}$, $P_\theta(\theta) = \frac{H_\theta(\theta)}{\sin\theta}$, $P_\varphi(\varphi) = H_\varphi(\varphi)$. The obtained interaction potentials were subsequently smoothed and tabulated for use in the CG simulations.

In cases where the proper dihedral distribution in the CG model, $P_\varphi(\varphi)$, does not agree well with the atomistic distribution $H_\varphi(\varphi)$, an additional dihedral refinement was performed on the concerned dihedral by running a 10 iteration IBI protocol on the dihedral following the protocol outlined below. This was done for the A-T-A2-G dihedrals of BTST and P2512, as shown in Figure 1, linking the spiro group to the central triazine ring, as well as for the D-A-A-D dihedral of mCBP.

The Non-Boded Pair Interactions were Parametrized Using the Iterative Boltzmann Inversion Scheme, with the Potential Updated as

$$U^{(n+1)} = U^{(n)} + \alpha \Delta U^{(n)}, \ \Delta U^{(n)} = k_B T_{\text{param}} \ln \frac{g^{(n)}(r)}{g_{\text{ref}}(r)} \tag{3}$$

Here, $g^{(n)}(r)$ is the CG pair correlation function at the n-th iteration step, $g_{\text{ref}}(r)$ is the pair correlation of the atomistic reference system mapped to a CG resolution, and $\alpha = 0.5$ is a scaling parameter. At every second iteration step a simple pressure correction was applied to the system by linearly perturbing the pair potential by $\Delta U_{PC} = -A(1 - r/r_c)$, where $A = -\text{sign}\Delta P \times 0.1 k_B T \min(1, f\Delta P)$, $\Delta P = P_i - P_{\text{target}}$, and $f = 0.001$.

For each compound, the pair interactions between all CG bead types were parametrized excluding contributions from non-bonded interactions within the same molecule. This means that for TMBT with two CG bead types, three different non-bonded interactions were parametrized. The IBI was performed with 200 iteration steps and a system size of 3000 molecules, where the initial configuration corresponds to the AA density. All non-bonded CG potentials were considered to be short-ranged and a cutoff of $r_c = 1.3$ nm was used when parametrizing these interactions. At each iteration step, a 400 ps CG *NVT* simulation was performed to obtain the updated pair interaction potential $g^{(n)}(r)$. This was done using the GROMACS 2019.3 package with a time step of 2 fs and the velocity rescaling thermostat with a time constant of 0.5 ps.[37,42,43,44]

To obtain the reference atomistic systems for CG force field parametrization an initial random configuration of 3000 molecules was generated using packmol.[45] The systems were then annealed at 800 K in the *NPT* ensemble before linearly cooling to the CG parametrization temperature T_{param} with a cooling rate of 10^{11} Ks^{-1}. Once at T_{param} the slab was then equilibrated for 10 ns in the *NPT* ensemble, followed by an additional 20 ns *NVT* production run. The final 15 ns of the production run were then used as the basis for the CG parametrizations. The parametrization temperatures T_{param} were chosen to correspond to the temperature 100 K above the AA glass transition temperature T_g^{AA} see Table 1.

To evaluate the CG models 20 ns *NVT* runs were performed with the CG force field at the parametrization temperature T_{param}. An additional 20 ns *NVT* run was also performed using bond constraints and the 4th order LINCS algorithm.[38] This was done as it allows the time step to be increased, making it possible to probe longer physical time scales without any significant increase in computational time.

Bonded and non-bonded distributions from the final 15 ns of both the unconstrained and constrained *NVT* runs were then compared to the atomistic distributions. For all the studied compounds both the constrained and unconstrained models reproduced pair correlations well,

confirming that the IBI procedure converged well in the CG models. Bond distributions in the unconstrained CG model, $P_r(r)$ and proper dihedral distributions, $P_\varphi(\varphi)$, also reproduce the atomistic distributions $H_r(r)$ and $H_\varphi(\varphi)$ well. However, in the case of the angle and improper dihedral distributions, while the agreement was generally good, some CG distributions were narrower with a higher peak intensity, than their atomistic counterparts. This was due to coupling between different bonded interactions and can be corrected by scaling the CG potentials. As the aim of this work was to develop a simple scheme for parameterizing CG force fields to accurately predict film morphologies as part of a high throughput screening process these slight discrepancies between the AA and CG models were deemed acceptable.

Glass Transition Temperature: T_g^{AA} and T_g^{CG} were determined by annealing a 3000-molecule system from 800 to 0 K in 8 ns in the *NPT* ensemble, giving a cooling rate of 10^{11} K s^{-1}. For the CG systems, bond constraints were applied allowing to use a time step of 10 fs. For the CG systems a slower cooling rate of $\Gamma = 10^{10}$ K s^{-1} was employed, other MD parameters were kept consistent with those used for the atomistic simulations. To determine T_g the density-temperature curves were fitted using bilinear fits.[21] As the computationally accessible cooling rates were typically several orders of magnitude faster than those utilized in experiments, it was expected that the simulated T_g^{AA} values will overestimate the experimentally determined ones.

For determination of the glass transition temperature at Merck KGaA, Darmstadt, Germany, differential scanning calorimetry (DSC) analyzing powder samples of 5 mg ± 10% were used in DSC 204 F1 Phönix from Netzsch. Samples were heated by 5 °C min^{-1} up to 370 °C then cooled by 20 °C min^{-1} to 0 °C and finally heated again by 20 °C min^{-1} to 370 °C, where T_g^{exp} was determined by the kink in heat flow versus temperature using the temperature corresponding to half the drop in heat flux. Only for BCP and TMBT, this protocol did not yield a significant kink. TMBT was expected to be the lowest T_g^{exp} material from simulation, so other protocols were tried to measure T_{gg}. It finally used a 5 mg TMBT sample in DSC Discovery from TA Instruments in nitrogen atmosphere and first heated by 20 °C min^{-1} up to 320 °C, then for cooling, quenched the sample by liquid nitrogen and finally heated by 20 °C min^{-1} up to 320 °C, where the Tg was observed. Other protocols for TMBT that were tried without the cooling quench did not lead to observation of T_g.

Refractive Indices: Refractive indices were measured for films with a thickness a 25, 50, and 75 nm using an M2000U ellipsometer from J.A. Woollam. The measurements were taken for three films across a range of thicknesses to avoid influence from sample defects. The obtained spectroscopic data were subsequently analyzed using the CompleteEase software package. The measured films were prepared by evaporation on a quartz substrate.

The refractive indices of the deposited CG films were calculated by first reintroducing atoms into the CG structures. To do this, it first inserts atomistic fragments into the CG structure, according to Figure 1, such that the centers of mass of the fragments were aligned with the corresponding CG bead positions. This was done with the csg_backmap calculator of VOTCA (https://gitlab.mpcdf.mpg.de/votca/votca). The initial AA structure was then relaxed by four cycles of energy minimization with GROMACS using the original AA force field.[42,43,44] In each energy minimization step, a steepest descent algorithm was employed with 10 000 relaxation steps. The first three cycles were restraint optimizations where virtual interaction sites were introduced at the CG bead positions. These virtual sites were pinned to their initial positions with a strong force constant to ensure that the original CG molecular structure was preserved. In the first energy minimization step, only bond, angular, and proper dihedral interactions were applied. This allows for an initial rotation of the fragments into the correct position. In the second step, all bonded interactions were switched on. The third step then introduces the non-bonded interactions, including electrostatic interactions. Finally, in the last energy minimization step the positional restraints were switched off giving a final deposited film with atomistic resolution. As the resulting AA structures were energy minimized structures they do not correspond to a statistical ensemble. This method had been found to yield adequate results for molecules of the size considered here, especially as the global orientation of molecules is, in this work, more important than a very high degree of accuracy in reproducing the statistical sampling of AA degrees of freedom.[46]

For every deposited AA film, the frequency-dependent relative permittivity tensor $\varepsilon_r(\omega)$ was calculated from molecular polarizabilities using the generalized Clausius-Mossotti relation. Defining the macroscopic polarization vector to be the sum of all individual induced dipoles of each molecule within the material and substituting it to the Clausius-Mossotti relation leads to the following matrix equation[47]

$$\left(\varepsilon_r - \hat{1}\right)\left(\varepsilon_r + 2\cdot\hat{1}\right)^{-1} = \frac{\bar{\alpha}}{3V\varepsilon_0} \tag{4}$$

where $\bar{\alpha}$ denotes the sum of the frequency-dependent molecular polarizability tensors over all N molecules within the volume V, $\bar{\alpha} = \sum_n^N \alpha^{(n)}(\omega)$. To evaluate the polarizability tensors of every molecule a dipole interaction model (IM-SQRT) was used suggested by Jensen et al.,[24] a more accurate variant of the Thole model. The atomic polarizabilities α_p, damping parameters ϕ_p and evolution parameters $\bar{\omega}_p$ needed for the IM-SQRT model were atom-type specific quantities and taken from Jensen et al.[24]

The simulated deposition of the films were done using a box with periodic boundary conditions in the *xy*-plane in which the molecules were inserted until the film reaches a desired thickness in the *z*-direction. To avoid effects of the surface due to the deposition several layers of molecules were cut from the two surfaces in the *z*-direction before analyzing the film. The volume V under consideration in Equation (4) was then determined by the box size in the x and y directions and the remaining thickness. This film slice of ≈1000 molecules had a height of ≈10 nm. The relative permittivity tensor was calculated at 620 nm, which was the experimentally used wavelength.

Based on the relative permittivity, one can then calculate the ordinary refractive index n_o within the *xy*-plane and the extraordinary refractive index n_e in *z*-direction perpendicular to the *xy*-plane, $n_o = \sqrt{(\varepsilon_{r,xx} + \varepsilon_{r,yy})/2}$, $n_e = \sqrt{\varepsilon_{r,zz}}$. n_o and n_e are frequency-dependent due to the components of $\varepsilon_r(\omega)$. By defining $\Delta n = n_e - n_o$ one then has a measure of anisotropy of the atomistic structures: a positive value of Δn corresponds to a standing upright conformation and a negative value of Δn corresponds to a lying flat conformation of the molecules. The Δn value, and associated error, for each compound were then calculated by considering the average of the five independent films. For the associated error we have chosen to also consider the error due to the temperature fluctuation of the film, $\sigma_{\Delta n,T}$ giving a total error of $\sigma^2_{\Delta n,tot} = \sigma^2_{\Delta n,T} + \sigma^2_{\Delta n}/5$.

Deposition: To conduct the CG deposition simulations a system of 1000 molecules was prepared by extracting the morphology at T_{dep}^{CG} from *NPT* cooling runs. Following an energy minimization, the simulation box was extended along the *z*-axis to a size of 45 nm, and the substrate was shifted upward by 2 nm in the box. This results in a slab which is used as the substrate. The positions of substrate molecules were frozen throughout the deposition simulation. The deposition itself was performed incrementally: In each deposition step four new molecules were inserted into the simulation box at a distance of 1.5 nm from the current substrate surface with an initial velocity of 0.25 nm ps^{-1} toward the substrate surface. These insertions were done by dividing the *xy* cross-section of the simulation box into a 4 × 4 grid of 16 cells. For each grid cell, the average CG number density in *z*-direction was then determined and the new molecules were inserted, with random orientation, into the four grid cells with the lowest densities. This scheme prevents the formation of voids during the deposition process. Following the insertion of the new molecules, those which were being deposited, a short CG simulation was performed in the *NVT* ensemble, with bond constraints and a timestep of 10 fs, to allow the deposited molecules to diffuse across and into the film surface. The deposition simulation makes use of coupling to two separate temperature baths: one for the group of previously deposited molecules and the second one for the newly inserted, depositing molecules. In both cases, the thermostating was done using the velocity rescaling thermostat. However in the case of the already deposited molecules these were coupled to a

temperature bath held at the deposition temperature T_{dep}^{CG}. The depositing molecules were coupled to a higher temperature T_{sub}. This sublimation temperature was chosen such that the cooling rate was constant across all deposition simulations when the inserted molecules were cooled, at a constant rate, from the insertion temperature to the deposition temperature over the duration of the simulation. In this case, the chosen cooling rate was 10^{10} Ks^{-1} and the total simulation time was 10 ns. Thus the sublimation temperature corresponds to $T_{sub} = T_{dep}^{CG} + (10^{-8}\ s \times 10^{10}\ Ks^{-1})$. The insertion and equilibration were repeated until the desired number of molecules had been deposited.

Acknowledgements

Open access funding enabled and organized by Projekt DEAL.

Conflict of Interest

The authors declare no conflict of interest.

Data Availability Statement

The data that support the findings of this study are openly available in [deposition] at [https://gitlab.mpcdf.mpg.de/materials/deposition], reference number [1].

Keywords

molecular dynamics, molecular ordering, organic light emitting diodes, refractive index

Received: July 17, 2024
Revised: September 5, 2024
Published online: September 29, 2024

[1] G. Hong, X. Gan, C. Leonhardt, Z. Zhang, J. Seibert, J. M. Busch, S. Bräse, *Adv. Mater.* **2021**, *33*, 2005630.
[2] *Organic Light-Emitting Devices: A Survey*, Springer, New York, NY, **2004**.
[3] K. Liu, B. Ouyang, X. Guo, Y. Guo, Y. Liu, *Npj Flex. Electron.* **2022**, *6*, 1.
[4] F. Yang, Y. Huang, Y. Li, Y. Li, *Npj Flex. Electron.* **2021**, *5*, 30.
[5] A. Mondal, L. Paterson, J. Cho, K.-H. Lin, B. van der Zee, G.-J. A. H. Wetzelaer, A. Stankevych, A. Vakhnin, J.-J. Kim, A. Kadashchuk, P. W. M. Blom, F. May, D. Andrienko, *Chem. Phys. Rev.* **2021**, *2*, 31304.
[6] O. Sachnik, X. Tan, D. Dou, C. Haese, N. Kinaret, K.-H. Lin, D. Andrienko, M. Baumgarten, R. Graf, G.-J. A. H. Wetzelaer, J. J. Michels, P. W. M. Blom, *Nat. Mater.* **2023**, *22*, 1114.
[7] P. Friederich, F. Symalla, V. Meded, T. Neumann, W. Wenzel, *J. Chem. Theory Comput.* **2014**, *10*, 3720.
[8] V. Rühle, A. Lukyanov, F. May, M. Schrader, T. Vehoff, J. Kirkpatrick, B. Baumeier, D. Andrienko, *J. Chem. Theory Comput.* **2011**, *7*, 3335.
[9] C. Degitz, M. Konrad, S. Kaiser, W. Wenzel, *Org. Electron.* **2022**, *102*, 106439.
[10] S. S. Dalal, D. M. Walters, I. Lyubimov, J. J. de Pablo, M. D. Ediger, *Proc. Natl. Acad. Sci* **2015**, *112*, 4227.
[11] I. Lyubimov, L. Antony, D. M. Walters, D. Rodney, M. D. Ediger, J. J. de Pablo, *J. Chem. Phys.* **2015**, *143*, 94502.
[12] M. Stroet, S. Sanderson, A. V. Sanzogni, S. Nada, T. Lee, B. Caron, A. E. Mark, P. L. Burn, *J. Chem. Inf. Model.* **2023**, *63*, 2.
[13] D. Yokoyama, Y. Setoguchi, A. Sakaguchi, M. Suzuki, C. Adachi, *Adv. Funct. Mater.* **2010**, *20*, 386.
[14] Y. Esaki, T. Komino, T. Matsushima, C. Adachi, *J. Phys. Chem. Lett.* **2017**, *8*, 5891.
[15] S. Kmiecik, D. Gront, M. Kolinski, L. Wieteska, A. E. Dawid, A. Kolinski, *Chem. Rev.* **2016**, *116*, 7898.
[16] G. D'Avino, L. Muccioli, F. Castet, C. Poelking, D. Andrienko, Z. G. Soos, J. Cornil, D. Beljonne, *J. Phys. Condens. Matter* **2016**, *28*, 433002.
[17] C. Poelking, D. Andrienko, *J. Chem. Theory Comput.* **2016**, *12*, 4516.
[18] A. Stankevych, A. Vakhnin, D. Andrienko, L. Paterson, J. Genoe, I. Fishchuk, H. Bässler, A. Köhler, A. Kadashchuk, *Phys. Rev. Appl.* **2021**, *15*, 044050.
[19] W. Liu, D. Andrienko, *J. Chem. Phys.* **2023**, *158*, 094108.
[20] H. Fidder, J. Knoester, D. A. Wiersma, *J. Chem. Phys.* **1991**, *95*, 7880.
[21] K.-H. Lin, L. Paterson, F. May, D. Andrienko, *Npj Comput. Mater.* **2021**, *7*, 179.
[22] D. Andrienko, *J. Mol. Liq.* **2018**, *267*, 520.
[23] C. A. Angell, *Science* **1995**, *267*, 1924.
[24] L. Jensen, P.-O. Åstrand, A. Osted, J. Kongsted, K. V. Mikkelsen, *J. Chem. Phys.* **2002**, *116*, 4001.
[25] W. L. Jorgensen, D. S. Maxwell, J. Tirado-Rives, *J. Am. Chem. Soc.* **1996**, *118*, 11225.
[26] J. Tirado-Rives, W. L. Jorgensen, *J. Am. Chem. Soc.* **1988**, *110*, 1657.
[27] T. A. Manz, N. G. Limas, *RSC Adv.* **2016**, *6*, 47771.
[28] U. C. Singh, P. A. Kollmann, *J. Comput. Chem.* **1984**, *5*, 129.
[29] V. Ruhle, C. Junghans, A. Lukyanov, K. Kremer, D. Andrienko, *J. Chem. Theory Comput.* **2009**, *5*, 3211.
[30] W. L. Jorgensen, J. Tirado-Rives, *Proc. Natl. Acad. Sci.* **2005**, *102*, 6665.
[31] D. J. Cole, J. Z. Vilseck, J. Tirado-Rives, M. C. Payne, W. L. Jorgensen, *J. Chem. Theory Comput.* **2016**, *12*, 2312.
[32] A. Tkatchenko, M. Scheffler, *Phys. Rev. Lett.* **2009**, *102*, 073005.
[33] M. J. Frisch, G. W. Trucks, H. B. Schlegel, G. E. Scuseria, M. A. Robb, J. R. Cheeseman, G. Scalmani, V. Barone, G. A. Petersson, H. Nakatsuji, X. Li, M. Caricato, A. V. Marenich, J. Bloino, B. G. Janesko, R. Gomperts, B. Mennucci, H. P. Hratchian, J. V. Ortiz, A. F. Izmaylov, J. L. Sonnenberg, D. Williams-Young, F. Ding, F. Lipparini, F. Egidi, J. Goings, B. Peng, A. Petrone, T. Henderson, D. Ranasinghe, et al., Gaussian 16, Version B.01 Gaussian, Inc., Wallingford CT, **2016**.
[34] S. Li-Ying, W. Xiao-Ming, H. Yu-Lin, D. Mu-Sen, Y. Shou-Gen, Z. Jia-Jin, *Acta Phys.-Chim. Sin.* **2012**, *28*, 1497.
[35] C. Bannwarth, et al., *WIREs Comput. Mol. Sci.* **2020**, *11*, e01493.
[36] H. J. C. Berendsen, J. P. M. Postma, W. F. Gunsteren, A. DiNola, J. R. Haak, *J. Chem. Phys.* **1984**, *81*, 3684.
[37] G. Bussi, D. Donadio, M. Parrinello, *J. Chem. Phys.* **2007**, *126*, 14101.
[38] B. Hess, H. Bekker, H. J. C. Berendsen, J. G. E. M. Fraaije, *J. Comput. Chem.* **1997**, *18*, 1463.
[39] W. Tschöp, K. Kremer, J. Batoulis, T. Bürger, O. Hahn, *Acta Polym.* **1998**, *49*, 61.
[40] F. Müller-Plathe, *ChemPhysChem* **2002**, *3*, 754.
[41] D. Reith, M. Pütz, F. Müller-Plathe, *J. Comput. Chem.* **2003**, *24*, 1624.
[42] M. J. Abraham, T. Murtola, R. Schulz, S. Páll, J. C. Smith, B. Hess, E. Lindahl, et al., *SoftwareX* **2015**, *1*, 19.
[43] B. Hess, C. Kutzner, D. V. D. Spoel, E. Lindahl, *J. Chem. Theory Comput.* **2008**, *4*, 435.
[44] S. Pronk, S. Páll, R. Schulz, P. Larsson, P. Bjelkmar, R. Apostolov, M. R. Shirts, J. C. Smith, P. M. Kasson, D. van der Spoel, B. Hess, E. Lindahl, *Bioinformatics* **2013**, *29*, 845.
[45] L. Martínez, R. Andrade, E. G. Birgin, J. M. Martínez, *J. Comput. Chem.* **2009**, *30*, 2157.
[46] M. Stieffenhofer, C. Scherer, F. May, T. Bereau, D. Andrienko, *Front. Chem.* **2022**, *10*, 982757.
[47] P. Palffy-Muhoray, *Chem. Phys. Lett.* **1977**, *48*, 315.